Nanoscale

ROYAL SOCIETY OF CHEMISTRY

PAPER

View Article Online
View Journal | View Issue

Check for updates

Cite this: *Nanoscale*, 2025, **17**, 8836

Synergistic effects of europium doping on MOF-5: exploring its photoluminescent and non-linear optical behaviour for enhanced optical limiting†

Selva Boopalan A,[a] Mani Rahulan K,[a] Angeline Little Flower N,[a] A. Dhanusha,[b] Sabari Girisun T C[b] and Annie Sujatha R*[a]

Received 23rd November 2024,
Accepted 23rd February 2025

DOI: 10.1039/d4nr04931d

rsc.li/nanoscale

Metal–organic frameworks (MOFs) are researched widely for their linear optical properties, while their non-linear optical (NLO) properties are rarely investigated. This report discusses the behaviour of MOF-5 and its ability to bond with a europium moiety to exploit its NLO properties using the *Z*-scan technique. A partial deterioration in the Raman spectra and quenching of light in the PL spectra in some samples emphasised the need to study their ability to exhibit phosphorescence. TR-PL analysis revealed nanosecond lifetime values, which were attributed to their ability to fluoresce owing to the weak bonding between the 1,4-benzenedicarboxylic linker and europium ions. The same deterioration was found in the non-linear absorption studies for these samples. Enhanced structural and optical properties were found in the 1% doped sample (M_1) that exhibited a reverse saturable absorption (RSA) in the *Z*-scan technique, which led us to find its optical limiting threshold (1.53×10^{12} W m^{-2}) and non-linear absorption coefficient ($\beta = 2.12 \times 10^{-10}$ mW^{-1}). An intensity-dependent non-linear absorption study revealed the presence of sequential two-photon absorption. These cumulative findings emphasize the potential of Eu^{3+}-doped MOF-5 as a promising material for NLO applications, with the M_1 sample demonstrating the best optical performance amongst the pure and doped MOF-5 samples.

1. Introduction

A non-linear optical phenomenon occurs, when a material is placed in the path of a strong coherent light source (LASER) which has been gaining interest in the field of optics, creating an intertwined path with the growing field of materials science leading to the development of novel non-linear optical materials. Non-linearity was first studied by Franken, who verified the second harmonic generation interaction,[1] which paved the way to further study the properties of NLO and unravel some of the important properties, such as third harmonic generation,[2] ultrafast photonics[3–5] and stimulated Raman scattering. With the introduction of non-linearity, several materials with non-linear behaviours were explored, thereby introducing materials like metal dichalcogenides,[6] r-GO composites,[7] transparent conductive oxides[8] and phosphates.[9] To overcome some of the disadvantages exhibited by inorganic materials, organic materials with large π-conjugated structures that provide the necessary intramolecular carrier mobility[10] were introduced into the field of NLO. During the investigations on organic materials, Yaghi introduced a new class of hybrid porous materials, namely, metal organic frameworks, in the late 1990s;[11] they were made up of infinite frameworks of organic linkers and metals and exhibited the coalescence properties of both the organic and inorganic moieties. Yaghi's continuous works were dedicated to the exploration of MOF structures based on some of his theoretical works.[12] Researchers started unravelling their most intricate properties, making them useful in applications like hydrogen storage,[13] gas adsorption,[14,15] catalysis[16] and drug delivery.[17] Some of their properties like tunable porosity[18] and large surface area[19,20] made them promising materials to work with. The aromatic linker groups are materials that can largely fluoresce. The active sites found in the organic linkers reveal some of the luminescence properties of the MOFs.[13] The linkers being the bridge for bringing out luminescence, the search for a co-material that has good chemical stability[21] and provides thermal resistance when energised was challenging. The doping or introduction of different functional groups to the MOFs results in the replacement of metal ions with the new

---

[a] *Nanophotonics Research Laboratory, Department of Physics and Nanotechnology, SRM Institute of Science and Technology, Chengalpet-603203, India. E-mail: anniesujatha@gmail.com*

[b] *Nanophotonics Laboratory, School of Physics, Bharathidasan University, Tiruchirapalli-620 024, India*

† Electronic supplementary information (ESI) available: EDS, FTIR, Raman, and TR-PL spectra. See DOI: **https://doi.org/10.1039/d4nr04931d**

doped functional group, which can enhance their stability and structure or otherwise.[22,23] This can enhance certain applications, such as photocatalysis,[24–27] gas separation[28] and gas transportation.[29] We mainly study the adaptability of the foreign material with the existing materials. Rare earth metals as the beacon for optical applications, including laser optics, are materials that have good chemical stability and thermal resistance[30] and can couple with the linkers to provide better luminescence. The lanthanide ions exhibiting better luminescence properties have an issue with self-excitation caused by the smaller molar absorption co-efficient ε; consequently, weak light absorption occurs. Therefore, revealing the luminescent properties of the lanthanides is a challenge to achieve. Therefore, we use the concept of the antenna effect to overcome this issue. The organic ligand inside the complex can absorb light owing to the presence of an organic chromophore, which contains several intense bands that excite the lanthanide ions to provide luminescence. To confirm this, Crosby and Whan team studied the non-radiative transfer of energy between lanthanide ions and organic linkers.[31] Various tailored properties are exhibited by the Ln-MOFs due to ligand modification. The lanthanide-based MOFs used in optical imaging are attributed to their luminescence properties.[32]

Hetero-metallic MOFs (lanthanide-doped MOFs) can be a challenge to attain because of the competition between rare-earth and transition metals for bonding with the organic linkers.[33] If the linkers are not properly bridged with the lanthanides, quenching can occur owing to the non-radiative decay, causing a decrease in the intensity of fluorescence or phosphorescence emission. Hence, combining a luminescent material with natural porous MOFs is a technical challenge but can be attained through a proper synthesis protocol.

Choosing a suitable synthesis method is an important factor because the metal organic framework can be adjusted for its topologies, stability, bonding and pore diameter by modifying the reaction conditions. Because there are diverse synthesizing strategies at present and many direct synthesis methods, such as hydro-/solvo-thermal method,[34] mechano-/sono-chemical method,[35] and microwave-assisted method,[36] the solvothermal method exists as a predominant method to synthesize MOFs, which can adjust reaction conditions, such as temperature, time, pressure and solvents, so that the surface areas and pore diameter of the MOFs can be minutely adjusted and maintained. Solvothermal approach, which involves dissolving organic solvents and metal salt in a specific solvent under controlled temperature and pressure conditions, specifically improves the nucleation and growth of MOF crystals and the dopants, thereby ensuring their interaction.[34] Rare earth metals contain partially filled 4f electrons, which have 5s and 5p electrons to shield them from the external environment, providing narrow emissions and absorption bands that make them suitable materials for producing monochromatic light. A material with high quantum efficiency, narrow emission bands and red luminescence is chosen to provide the luminescence, while a well-established and stable material with a cost-effective synthesis method is chosen as the core material. Europium and MOF-5 are chosen as the dopant and inorganic–organic moiety to study their luminescence properties and non-linear behaviour. MOF-5 is a 3-dimensional metal complex that has inorganic moiety as Zn_4O clusters and organic linker as 1,4-benzendicarboxylic acid (1,4-BDC), which demonstrates wide surface area, large pore volume and good thermal stability.[37] Yaghi and co-workers studied the open framework structure of MOF-5[12] and synthesised a lanthanum–organic framework[38] that gave an idea to use the lanthanum ions to increase the efficiency of MOF-5. The ability to control the pore size and the linkers makes it a viable candidate for many applications, including energy storage.[39] Using the solvothermal synthesis route, better coordination control can be gained over europium within the MOF-5 structure, which facilitates its bounding and precise positioning within the framework and retains the large surface area and porosity of MOF-5.[34]

MOF-5 is largely used in the applications related to gas adsorption and separation owing to its large surface area and ability to tune its porosity. Studies conducted by Botas and co-workers on the adsorption properties of MOF-5 on gases such as hydrogen (at 77 K), methene (at 273 K) and carbon-dioxide (at 273 K) showed higher adsorption capacities at higher pressure, and the incorporation of cobalt (doping) showed a slight increase in the adsorption properties.[40] Ozen and co-workers studied the gas permeability of hydrogen, methene and carbon-dioxide using MOF-5 as the dopant in polyimide membrane, which showed single gas permeation for these gases that increased upon the incorporation of MOF-5 at room temperature and 200 kPa pressure.[28] Patil and co-workers worked on functionalizing graphite oxide quantum dots onto MOF-5 through a surface modification doping strategy. Owing to its improved electron-donating and surface properties, it provides high-performance TENG devices.[41] Tang and co-workers studied phosphor coated white light emitting diodes using lanthanum-MOFs because of the antenna effect.[42] Ren and co-workers introduced perovskite quantum-dots into MOF-5 to develop green light emitting diodes.[43]

Therefore, we discuss a synthesis protocol for MOF-5, followed by the doping of europium using the solvothermal method, and its structural, morphological, linear optical and non-linear optical studies are also discussed.

2. Experimental section

Materials

Zinc(II) nitrate hexahydrate [$Zn(NO_3)_2{\cdot}6H_2O$, Sisco Research Laboratories Pvt., Ltd, extrapure AR, 98%], benzene-1,4-dicarboxylic acid or terephthalic acid (1,4-BDC, $C_8H_6O_4$, Sisco Research Laboratories Pvt., Ltd, pure, 98%), triethylamine, europium(III) nitrate pentahydrate [$Eu(NO_3)_2{\cdot}5H_2O$, Sisco Research Laboratories Pvt. Ltd extrapure AR, 99%], and *N*,*N*-dimethylformamide [DMF, Sisco Research Laboratories Pvt. Ltd Dried, 99.5%]. All the reagents used were of laboratory grade and used without further purification.

Synthesis of MOF-5 (Fig. 1)

Zinc Nitrate Hexahydrate (ZNH) (1.086 g, 3.62 mmol) dissolved in *N*,*N*-dimethylformamide (DMF) (25 mL), and benzene-1,4-dicarboxylic acid (1,4-BDC) (0.334 g, 1.19 mmol) dissolved in *N*,*N*-dimethylformamide (DMF) (25 mL). Then, triethylamine (TEA) (0.5 mL) was dropwise added to the 1,4-BDC solution. Both solutions were stirred separately for 30 min at 60 °C.[33] The prepared 1,4-BDC solution was slowly added to the prepared ZNH solution. The clear solution ZNH turned from a transparent solution to a pale white precipitate with the addition of a 1,4-BDC solution.

Synthesis of Eu^{3+}-doped MOF-5

Three sets of solutions (Fig. 1) were prepared with ZNH solution (3.62 mmol) and a 1,4-BDC linker (1.19 mmol) in DMF (25 mL) separately and stirred for 30 min. The protocol described previously was followed. After 30 min, 1,4-BDC solution was added to the ZNH solution with TEA (0.5 mL) and 1% (0.0108 g), 2% (0.0216 g), and 3% (0.0324 g) of europium(III) nitrate pentahydrate were added to the respective solution while stirring at 60 °C. All the four solutions (MOF-5 (**M_0**), 1% doped MOF-5 (**M_1**), 2% doped MOF-5 (**M_2**), and 3% doped MOF-5 (**M_3**)) were stirred at 60 °C. After an hour, the solution showed a white precipitate. The pH was maintained at 7, and the viscosity of the solutions was determined to be 0.761 cP. They were poured into 100 mL Teflon containers separately and heated to 100 °C for 30 hours with 5 °C per minute rising temperature, after which they underwent the nucleation process (Fig. 2). The Teflon was rapidly cooled to room temperature, and samples were taken out of the 100 mL Teflon container and washed. The prepared samples were centrifuged thrice with DMF and allowed to dry at 80 °C for 24 hours, after which the powder was calcined for 3 hours at 250 °C with a 5 °C per minute rising temperature. The resulting powder samples were collected with a total yield of **~0.850 g**. The bonding (Fig. 3) between the pure and doped samples was studied using various characterisation methods.

Z-Scan setup

The NLA was studied using the OA *Z*-scan method (Fig. 1) with a Q-Switched Nd:YAG pulsed laser with a 9 nanosecond pulse width and a 10 Hz repetition rate, which is operated at a 532 nm wavelength. The pulses converged using a plano-convex lens of 150 mm focal length to intensify the beam at the centre ($Z = 0$). The beam remains nearly diffraction-limited with 1.69 mm of Rayleigh range and a path length of cuvette being 1 mm. The samples were dispersed in *N*,*N*-dimethylformamide (η = 1.43). The cuvette with the dispersed sample was mounted over a motorized (automated) translation stage and allowed to move along the path of the converged (focal region) beam. The transmittance is measured and plotted against the axial position.

3. Results and discussion

XRD analysis

The grain size and crystallinity of the pure and doped metal organic framework are characterized using the powder-XRD patterns acquired from the XRD data (Fig. 4). The crystal planes **(220)**, **(440)**, **(420)**, **(333)**, and **(440)** affirm the nucleation of MOF-5 and correlate with the diffraction peaks corresponding to the 2θ values of 9.76, 14.58, 15.53, 17.50, and 19.16, respectively, which is in accordance with the JCPDS file **(JCPDS-96-410-9208)**. The diffraction peak observed at 8.97 can

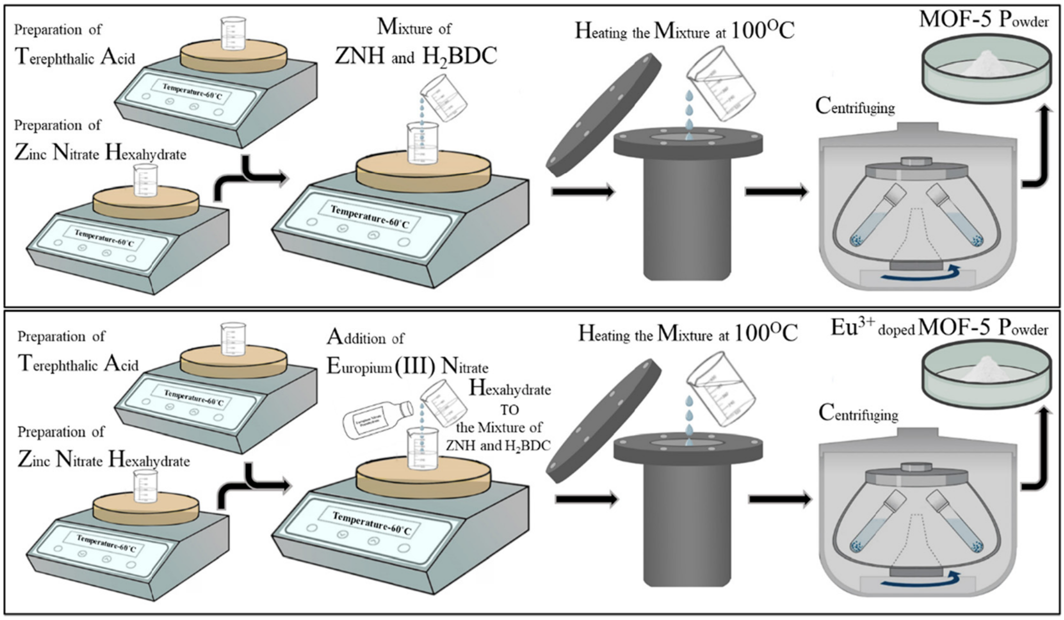

Fig. 1 Graphical representation of the synthesis protocol for pure and doped MOF-5 samples.

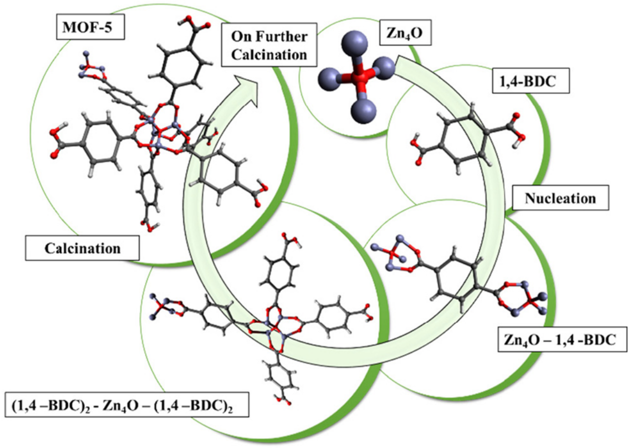

Fig. 2 Graphical representation of the nucleation process of MOF-5.

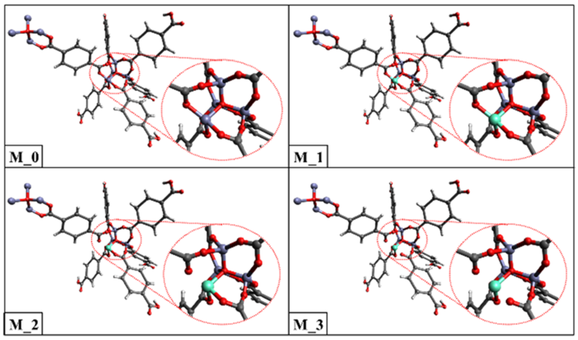

Fig. 3 Graphical representation of bonding between 1,4-BDC linker and Eu^{3+} ions of the pure and doped MOF-5.

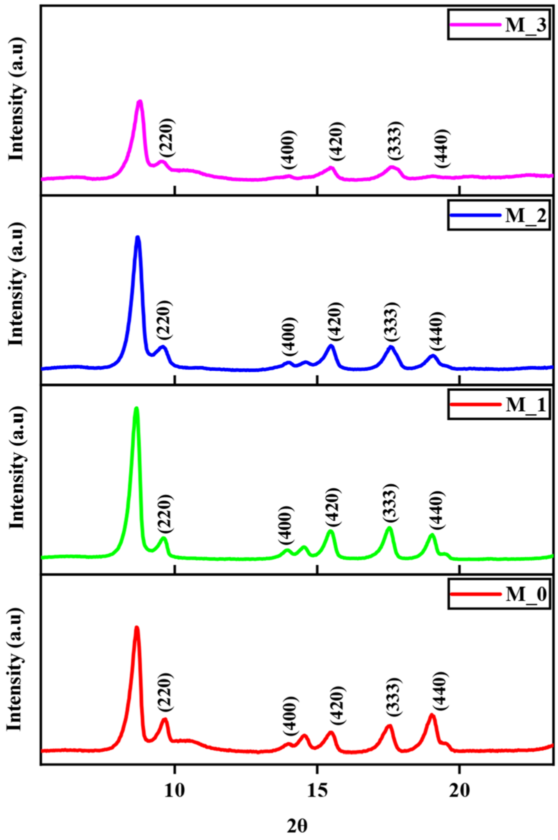

Fig. 4 Powder XRD patterns observed for the pure and doped MOF-5 samples.

be attributed to the presence of atmospheric moisture,[44] and owing to the presence of moisture, a partial distortion can be found, which was also observed by Hausdorf and co-workers.[45] Consequently, a phase shift is found in the crystal structure from cubic to trigonal, with an $R\bar{3}m$ space group[46] having 23.514 nm lattice parameter a. The 9.76 peak undergoes splitting, and a decrement in the intensity of the peaks is observed; similar characteristics were observed in the studies conducted by Lillerud and co-worker, attributed to the distortion in the cubic structure.[46] The M_1-doped samples show an increase in intensity, while the M_2- and M_3-doped samples show a decrease in intensity, as observed by Dhara and co-workers.[47] The incorporation of Eu^{3+} into the MOF-5 structures results in the enhancement of certain crystallographic planes, causing the intensity of the XRD peaks to increase. The decrease in the peak intensities is attributed to the disruption in the planes caused by the distortion in the lattice, reducing regularity in the planes, which can be attributed to the large ionic size of the Eu^{3+} ion.[33] As we attempted to synthesize a hetero-metallic MOF, there was competition between the rare earth metal and the transition metal to bridge with the ligand. The successful incorporation of the Eu^{3+} ions leads to a saturation of defects, clustering of dopants and changes in the growth dynamics, which collectively contribute to an increase in crystallite size, while the failure to bond with the ligands disrupts the crystal growth process and results in a decrease in the crystallite size (Table 1).

The δ (Table 1) of the M_0 sample decreases as the concentration of the Eu^{3+} ion increases, thereby increasing the structural stability of the M_1 sample. However, as the concentration increases, the M_2 sample shows an increase in the δ indicated by the broadening of peaks, and a further increase in the concentration of the M_3 sample causes δ to increase, resulting in wider and more pronounced peak broadening. This leads to an increase in strain, which can cause defects in the crystal structure.[48] Similarly on calculating the lattice strain ε (Table 1) using the Williamson–Hall plot (Fig. S1†), it shows a decrease in strain for M_1, but a further increase in concentration in the M_2 and M_3 samples leads to an increase in strain, causing the structure to collapse, which is in accordance with the dislocation density found.[23] As the concentration increases in the M_2 sample, there is a decrease in the lattice parameter, attributed to the increased δ and ε.

The lattice parameter shows a slight increase for the M_1 sample from M_0, which is due to the presence of larger Eu^{3+} ions (ionic radius: 1.066 Å) replacing smaller Zn^{2+} ions (ionic radius: 0.74 Å) within the framework, which can lead to a slight expansion of the lattice. The mismatch (Eu^{3+} replacing

Table 1 Crystallographic information of the pure and doped samples found using the equations (refer to Table S1) and W–H plot (refer to Fig. S1†)

Sample	Average crystallite Size D (nm)	Dislocation density $\delta \times 10^{-3}$ (nm^{-2})	Lattice strain ($\varepsilon \times 10^{-3}$)	Lattice parameters a (nm)	Average grain size (μm)
M_0	21.507	2.161	4.57	23.519	1.941
M_1	26.246	1.451	1.22	23.549	1.556
M_2	22.568	1.963	3.75	23.485	2.066
M_3	20.689	2.336	8.31	23.739	2.200

Zn^{2+}) caused by the introduction of Eu^{3+} ions causes local lattice distortions and slight adjustments to accommodate the new ion, resulting in varied lattice parameters. Owing to localized strain, saturation effects and complex structural reorganization, the distortion can vary, leading to a non-linear relationship with the lattice parameter. The strain, which also depends on the Eu^{3+} concentration (clustering or preferential site occupancy), allows the lattice to adapt to the electronic environment and size of the dopant, leading to a non-linear variation in lattice size while increasing the Eu^{3+} concentration.[23] The re-organization of the structure to minimize the strain, leading to irregular changes in M_3 samples, can cause an increase in the Lattice parameters.

High resolution SEM

High resolution SEM images (Fig. 5) reveal the 3-dimensional cubic crystals of the pure and doped MOF-5 with sizes ranging from **~1.5 μm** and **~2 μm**. The cube-shaped morphologies exhibited by the pure and doped MOF-5 samples, which are similar to the studies conducted by M. Fiaz and co-workers, are observed.[44] The presence of secondary structures, such as nanoplates, was observed, which is the result of environmental conditions, such as time, as a single entity rather than separate shapes that are interconnected to the nature of MOF. The presence of randomly oriented connections of nanoparticles along with evenly distributed pores inside the cubes was observed, and when the reaction time was increased, we noticed the removal of some layered particles.[49] Cube-shaped morphologies found in the HRSEM images reveal that there are no significant changes found between the pure and doped samples. For accuracy, the grain size[50] (Table 1) was determined using ImageJ software, which averages the grain size of the cube-shaped structures in the HRSEM images (Fig. S2†). This, in turn, emphasises the decrease in the grain size of the M_1 sample compared to M_0 and an increase in the grain size of M_2 and M_3 compared to M_0. This explains the collapsed structure as the doping concentration increases, which is also in accordance with the XRD parameters (Table 1). This is also in accordance with studies conducted by Goktas and co-workers.[22] The EDS spectrum (Table S2†) and mapping (Fig. S3†) were used to study the spatial distribution of the elements present in the samples. Element composition (Table S2†) explains the partial deterioration in the structure for M_2 and M_3 samples with the increase in the weight percentage of Zn ions.

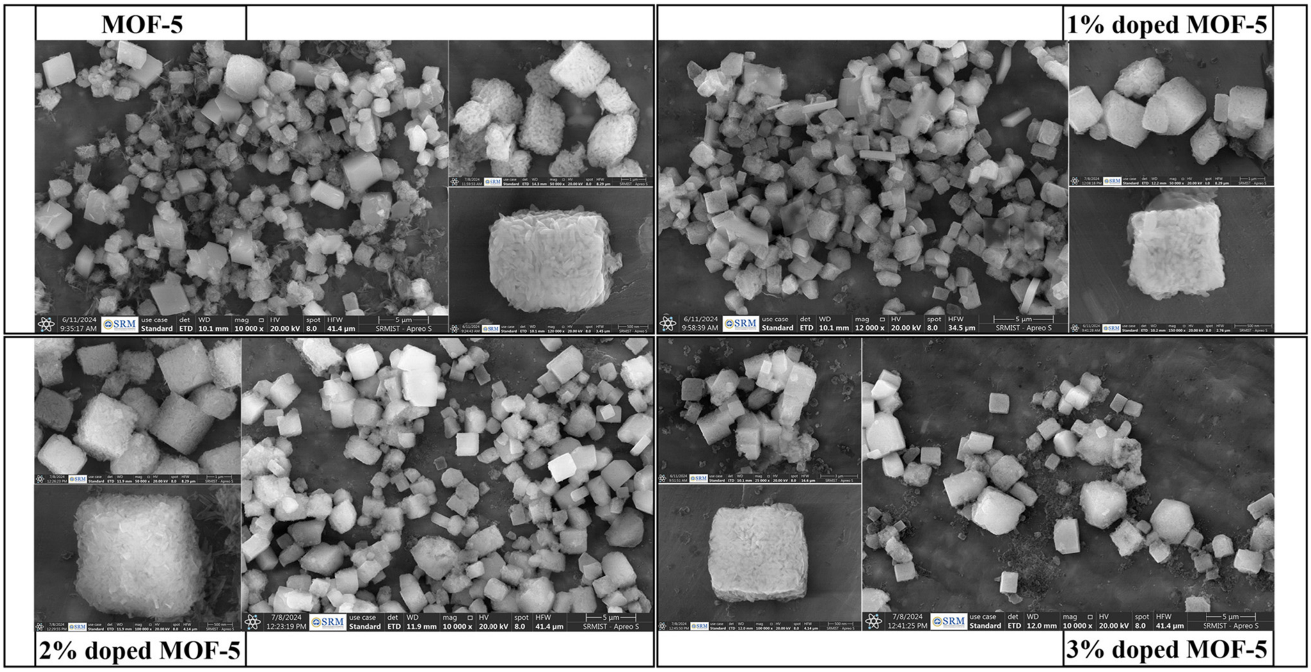

Fig. 5 High resolution-SEM images of pure and doped MOF-5.

X-ray photoelectron spectroscopy

The chemical state and elemental composition of the surfaces were analysed using X-ray photons, which penetrated the material surface to detect the electrons that show inelastic scattering, with a mean free path value between 0.5 nm and 3 nm. Spectral peaks are acquired by calculating the kinetic energy emitted by electrons. The survey spectra peaks (Fig. 6b) ascribed to the core levels of Zn 2p, Zn 3p, O 1s, C 1s and Eu 4d are found between 1100 eV and 0 eV, which reveals the presence of MOF-5 composition along with the presence of Eu^{3+} on the doped samples. The deconvoluted core spectra for Zn 2p (Fig. 6a) are found between 1054 eV and 1016 eV. A splitting of the peak into a doublet peak at 1045 eV and 1022 eV is observed, which is caused by the property of spin orbit coupling.[51] The 1045 eV and 1022 eV are attributed to Zn $2p_{1/2}$ and Zn $2p_{3/2}$, respectively, which explains the +2 oxidation state of the material. The auger peaks (Zn LMM) at 496 eV and 473 eV are observed (Fig. 6b),[52] which arises because of inelastic scattering. The absence of a shift in the auger spectrum reveals the absence of extra zinc on the surface of MOF-5 on doping Eu^{3+}. The peak at around 974 eV can be attributed to the Zn^{2+} cation in the MOF-5.[52] The deconvoluted XPS spectra for O 1s are found between 535 eV and 529 eV. The 531.4 eV is attributed to the C═O,[51] and the 530.4 eV addresses the adsorption of O_2 electrons to the surface.[52] The deconvoluted XPS spectra for C 1s are found between 293 eV and 281 eV. The 284.7 eV, 286.2 eV and 288.8 eV peaks are attributed to the presence of C–C, C═O, and O–C═O in the sample, respectively.[51] The Eu^{3+} $4d_{3/2}$ and Eu^{3+} $4d_{5/2}$ are the main features observed in the XPS spectra. As there is a very weak presence of Eu^{3+} 3d contributions, we collect high resolution XPS spectra of Eu 4d (Fig. 6c). The escape death of the 3d photoelectrons is smaller compared to that of 4d, and it can be used to study the surface sensitive information. The presence of Eu^{3+} $4d_{3/2}$ and Eu^{3+} $4d_{5/2}$ at 141.1 eV and 136.8 confirms the presence of a $^{3+}$ oxidation state.[53]

The increase in intensity of the Zn $2p_{1/2}$ and Zn $2p_{3/2}$ explains that the M_1 sample has a larger amount of Zn ions spread over the surface, while M_2 and M_3 have fewer Zn ions compared to the M_1 sample. The absence of 531.4 eV in the 1% doped samples can be attributed to the absence of C═O presence. The reduction in the 286.2 eV peak in sample M_1 can be attributed to the reduction in C═O, which is in accordance with the O 1s peak at 531.4 eV. The Eu $4d_{5/2}$ peak at 136.8 eV is blue shifted by ~2.2 eV for the M_2 and M_3 samples compared to the M_1 sample, which explains the change in bond distance between the Eu and O of the M_2 and M_3 samples.[53]

FTIR spectroscopy

The functional groups of the samples are analysed using FTIR spectroscopy. The spectra (Fig. S4†) reveal an important trans-

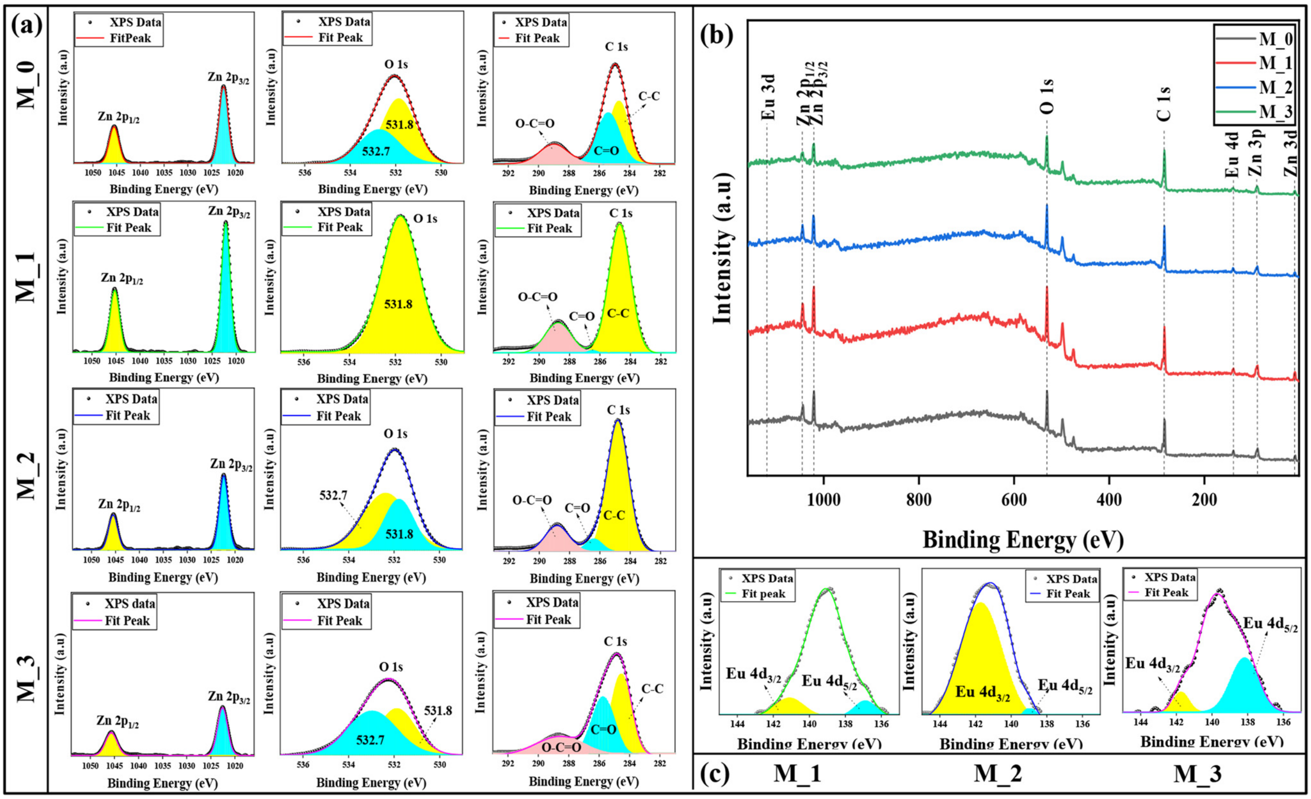

Fig. 6 XPS studies of (a) deconvoluted XPS spectra of Zn, O, and C, (b) survey spectra, and (c) Eu 4d deconvoluted XPS spectra for the pure and doped samples.

mittance peak at 1569 cm^{-1}, which can be referenced to the 1,4-BDC linker symmetric vibration. A reduction in intensity is observed compared with the free 1,4-BDC linkers, which confirms the coordination with the metal nodes.[16] The presence of asymmetric vibrations is denoted by 1372 cm^{-1} transmittance peaks, which are attributed to the C–H groups in the linker.[54] Absorption bands between the wavenumbers 600 cm^{-1} and 1200 cm^{-1} are called the fingerprint region for 1,4-BDC linker-based compounds, and the transmittance peaks found between 850 cm^{-1} and 600 cm^{-1} are attributed to the out-plane and in-plane stretching vibrations belonging to the C–H group of the benzene ring.[44] Deprotonation of the –COOH group from the terephthalic acid can be indicated by the absence of a strong peak between 1850 cm^{-1} and 1650 cm^{-1}.[55] The peak found at 649 cm^{-1} is attributed to the stretching vibrations of $[Zn_4O]^{6+}$.[56] The less intense transmittance peak found at 3605 cm^{-1} indicates the small amounts of DMF molecules even after annealing.[57] The broad band around 3200 cm^{-1} is caused by the O–H vibrations attributed to the presence of moisture, which is in accordance with the XRD data.[54]

Raman spectroscopy

Using a 532 nm source. Raman Spectroscopy, as the non-destructive method, was used to find vibrational modes using scattered light. From the Raman spectra (Fig. S5a†), we analyse the vibrational modes of the pure and doped MOF-5 samples, which are highly dominated by the vibrational modes of the organic moieties.[58] Upon excitation, we observe five major peaks, which can be attributed to the vibration modes of an aromatic benzene ring and –COO group of the 1,4-BDC linker. The reduction in the intensity and the changes found in the shape of the peaks can be attributed to the partial deterioration of the carboxylate group and the organic benzene ring.[59] The 1615 cm^{-1} is related to the vibrational stretching mode of the benzene ring, 1428 cm^{-1} occurs because of the stretching modes of the carboxylate groups, 1135 cm^{-1} is attributed to the breathing (simultaneous compression and stretching of C–C bonds) of the benzene ring, and 862 cm^{-1} is related to the benzene group's stretching that is the C=O bending of the carboxylate group.[59] The doped samples show low intensity peaks, which are dominated by the photoluminescence background.[58]

Using a 633 nm source. The Raman spectra (Fig. S5b†) for the pure and doped MOF-5 samples were studied using a 633 nm LASER source. The sample shows no big shift in the Raman spectra, but a slight red shift is found on the peaks compared to that of the 532 nm laser. A slight red shift in the 1440 cm^{-1} peak is found in the 2% and 3% doped samples, which can be attributed to the expansion in the lattice. Unlike 532 nm (green pulsed) LASER, 633 nm (red pulsed) LASER shows clear and visible Raman spectra for 2% and 3% doped samples.[59]

UV-visible spectroscopy

The linear absorption properties of the samples were studied using UV-visible spectroscopy, which gives the absorption spectra. The absorption spectra (Fig. 7) reveal the maximum absorption and the respective Tauc plots. A steep absorption edge is found at 350 nm for the pure and doped samples. The M_0 samples show maximum absorption at 288 nm, and a 2 nm shift (red shift) is absorbed for the doped MOF-5 samples, which can be attributed to the change in band structure caused by the dopant-induced lattice distortion.[60] From the absorption spectra of M_2 and M_3, we observed an extra band at 365 nm, and this was also verified in the studies conducted by Asadevi and co-workers,[54] indicating the presence of ZnO moieties with an absorption band of around 350–400 nm.[47] The maximum absorption found at 288 nm can be attributed to the π–π* transition occurring owing to the 1,4-BDC linker's π electrons.[52] This can be attributed to the transition of $1A_{1g}$ to $1B_{2u}$,[54] where $1A_{1g}$ represents the ground state or a singlet state, where all the electrons are paired with a gerade (even) symmetry and $1B_{2u}$ represents the excited state with ungerade (odd) symmetry. The extrapolated Tauc plot (eqn (1)) reveals a blue shift in the bandgap, from 3.81 eV to 3.78 eV, 3.70 eV, and 3.68 eV for the M_0 to M_1, M_2, and M_3 samples, respectively. The blue shift explains the partial deterioration of MOF-5 into ZnO owing to the doping of the Eu^{3+} ion:

$$(\alpha h\nu)^n = A_t(h\nu - E_\mathrm{b}), \tag{1}$$

where $h\nu$ is the photon energy, α is the absorption co-efficient, A_t is a constant, $n = (2)$ for direct band gap materials, and E_b is the optical band gap.

Photoluminescence spectroscopy

The emission spectra of pure and doped MOF-5 samples are studied using 288 nm as the excitation wavelength. The PL spectra (Fig. 8a) show a broad emission at 420 nm and a narrow sharp peak at 615 nm, representing the π–π* transition[61] of the 1,4-BDC linker and $^5D_0 \rightarrow {}^7F_j$ transition[62] of the Eu^{3+} ions. The broad emission peak found at 420 nm can be attributed to strong coupling and ligand-to-metal charge transfer (LMCT) arising between the electronic and vibrational modes of the 1,4-BDC linker.[62] Because the parity forbidden f–f transitions and europium ions have disadvantages such as low absorption co-efficient and weak luminescence intensity,[62] we introduced organic ligands, which are known for their antenna effect[63] that can compensate for the weak excitation of Eu^{3+} ions and allow them to luminesce properly. Sample M_1 (Fig. 9b) shows the maximum intensity attributed to the stability of the MOF-5 after the incorporation of Eu^{3+} ions. The transition found around 615 nm can be attributed to the hypersensitive transition occurring owing to the presence of $^5D_0 \rightarrow {}^7F_2$, and a neighbouring $^5D_0 \rightarrow {}^7F_1$ transition helps us unravel the symmetric nature of the material. An intense transition found at $^5D_0 \rightarrow {}^7F_1$ is attributed to a centrosymmetric environment, while an intense $^5D_0 \rightarrow {}^7F_2$ transition is attributed to a non-centrosymmetric environment of the material. The strong luminescence caused by the Eu^{3+} ions attributed to the sharp narrow peak at 615 nm is an electric dipole transition, and the less intense peak at 592 nm is a magnetic

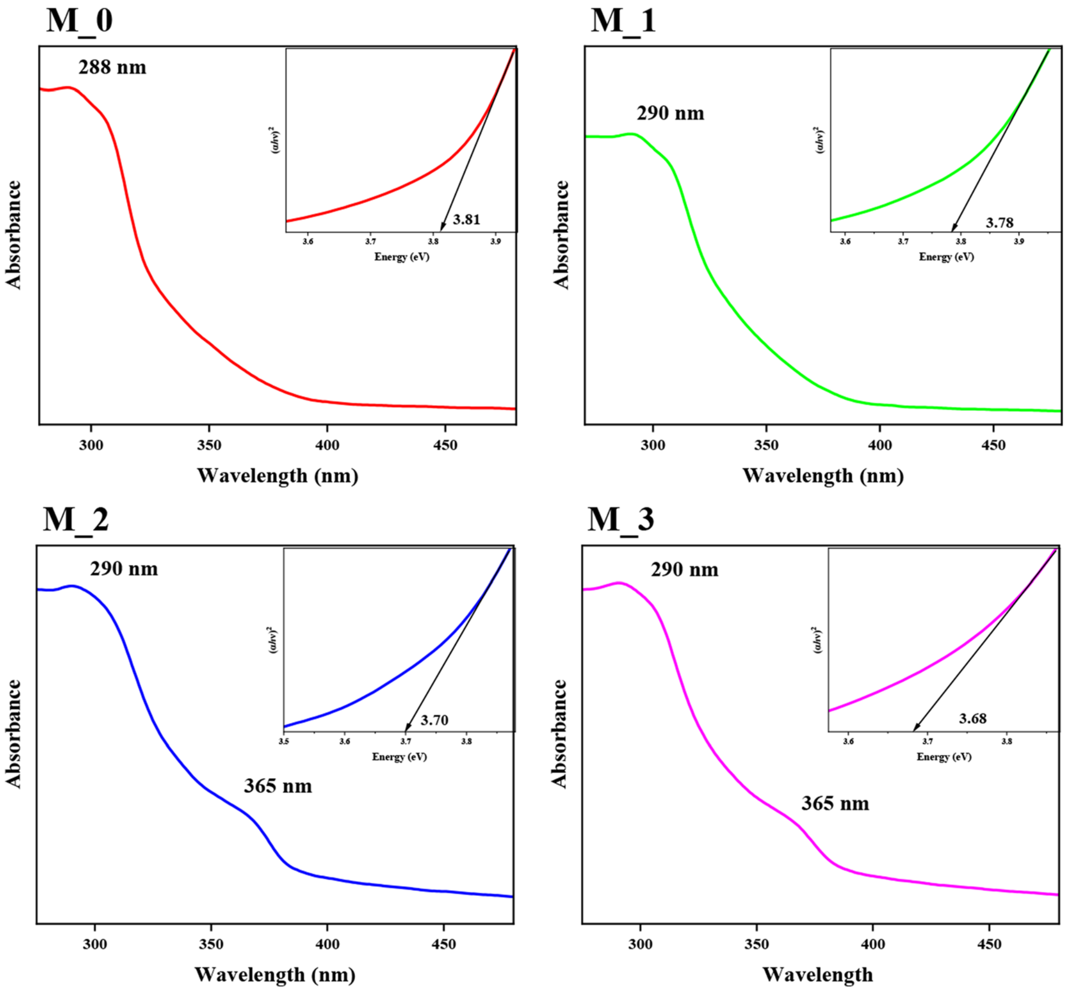

Fig. 7 UV-visible absorption studies for the pure and doped MOF-5 samples and their corresponding Tauc plots (insets).

dipole transition. According to Judd-Ofelt's theory, the presence of a weak 574 nm peak attributed to the presence of the $^5D_0 \rightarrow {}^7F_0$ transition can occur in only rare crystalline material with a non-centrosymmetric field of low symmetry, which proves that the pure and doped MOF-5 samples show low symmetry.[62] Hence, the material emits an intense red emission owing to the presence of a high intensity peak at 615 nm in the PL. The energy transfer occurring in the Eu^{3+} MOF-5 can be better understood using Jablonski's diagram (Fig. 9), which explains the energy transfer from MOF-5 *via* ligand to the Eu^{3+} ions. Photons absorbed by the MOF-5 molecules undergo excitation to the excited state (S_2) from the ground state (S_0) at 34 722 cm^{-1}. The internal conversion (IC), which is a non-radiative process, relaxes it to the lower excited state (S_1) from the higher excited state (S_2) without emitting photons at 23 809 cm^{-1}. Inter System Crossing (ISC) is another non-radiative process that relaxes it to the triplet state (T_1) to the lower excited state (S_1), which is a singlet state, and further to the ^7F_J transition (where J = 0 to 4) emitting a red light through $^5L_6$–$^5D_0$–^7F_J transitions.[63] A decrease in the intensity of the PL spectra in the M_2 and M_3 samples supports the partial deterioration theory found in the UV-visible analysis. The broadening of the emission peaks at 420 nm can also be attributed to the partial deterioration of the material.[64] The partial deterioration, which was not found in the high-resolution SEM and FTIR, may be attributed to the fact that the deterioration resulted from the defects present in the crystal structure, leading to quenching or trapping of light. The deterioration in the M_2 and M_3 samples is attributed to the quenching of light, which is verified using Time Resolved Photo-Luminescence (TR-PL) studies. The TR-PL spectra (Fig. S6†) are fitted using the bi-exponential function. To find the decay process for complex systems, such as the metal organic framework, we use a bi-exponential function that uses the faster decay component τ_1 and slowed decay component τ_2 to calculate the decay time. The lifetime of the samples falls in the nanosecond regime. Villemot and co-worker also had decay times in the nanosecond regime for MOF-5.[64] Because Eu^{3+} luminescence falls on the millisecond regime, the 1,4-BDC linker does not provide the necessary excitation, which means that the Eu^{3+} ion fails to properly bond with the 1,4-BDC, which can be caused by the competition between the tran-

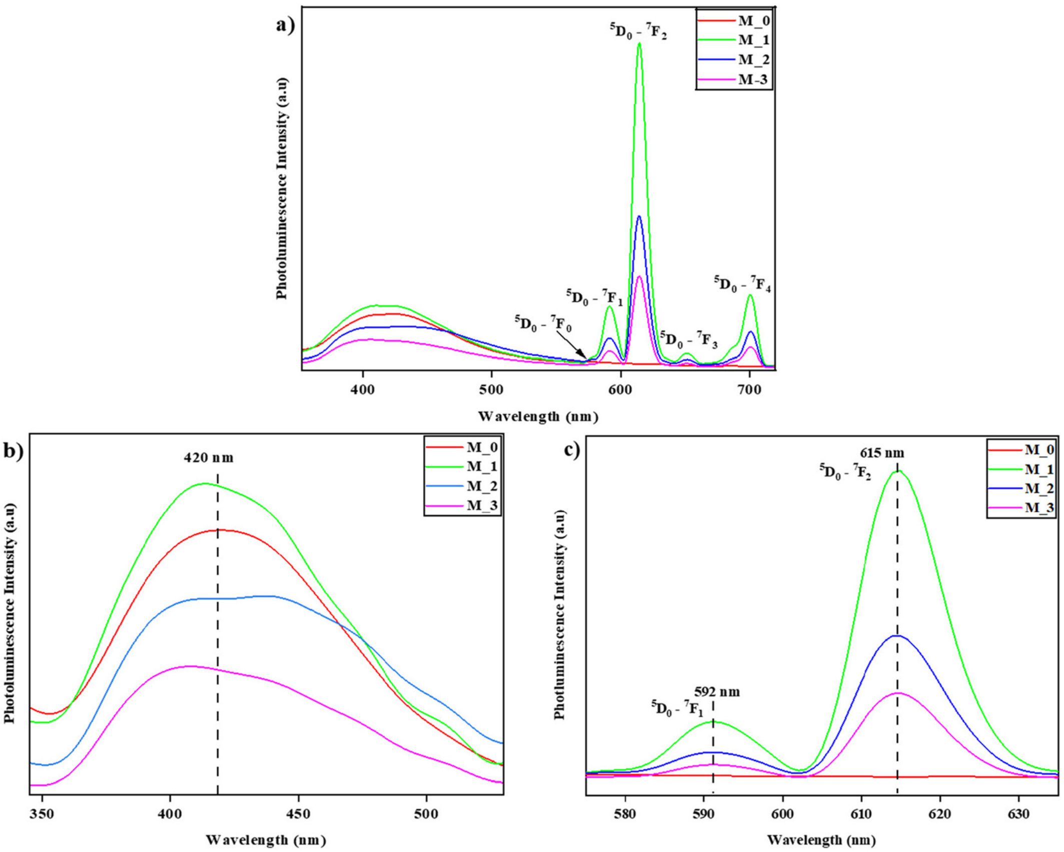

Fig. 8 (a) Photoluminescence spectra of the pure and doped samples, (b) PL Spectra of 1,4-benzene dicarboxylic acid, and (c) PL Spectra of Eu^{3+} ion.

sition metals during synthesis. Hence, the pure and doped samples exhibit only the fluorescence provided by the linker. Color coordinates of the pure and doped samples are plotted using a CIE diagram (Fig. S7†) using the emission spectra. The CIE diagram of the M_0 sample shows the blue emission and the M_1 sample shows a red emission, which is attributed to the red luminescence of Eu^{3+}, and further doping shifts the M_2 and M_3 samples to the violet emission, which is attributed to the partial deterioration.

Non-linear investigation using the *Z*-scan technique

Non-linear absorption co-efficient. Contrary to the absorption in the linear regime, the non-linear absorption increases along with the intensity of the beam. At the focal point, the spectra (Fig. 10) exhibited a decrease in transmittance, which is attributed to the pure and doped MOF-5 properties that exhibit reverse saturable absorption (RSA).[65] We find total non-linear absorption co-efficient α_A (eqn (2)), a sum of the negative and positive transmission coefficients. We find normalized transmittance T_Z (eqn (3)) using the Sheik Bahae's theoretical fit[66] to match the reverse saturable absorption data.

$$\alpha_A = \frac{\alpha_0}{1 + \frac{I}{I_{SI}}}\beta \times I, \tag{2}$$

where α_0 is the linear absorption coefficient, I is the laser intensity, I_{SI} is the saturation intensity, and β is the non-linear absorption co-efficient.

$$T_Z = \frac{1}{\left(1(n-1)\beta L_{eff}\left(\frac{I_0}{1+\left(\frac{Z}{Z_0}\right)^2}\right)^{n-1}\right)^{1/(n-1)}}, \tag{3}$$

where n is the order of the TPA non-linearity, I_0 is the intensity at focus, Z_0 is the Rayleigh range (eqn (4)), and L_{eff} is the effective length (eqn (5)).

$$Z_0 = \frac{\pi \omega_0{}^2}{\lambda}, \tag{4}$$

where ω_0 is the beam waist at focus and λ = 532 nm.

$$L_{eff} = \frac{(1 - \exp(-\alpha_0 L_p))}{(\alpha_A)} \tag{5}$$

where L_p is the path length of the dispersed sample and α_A is the linear absorption co-efficient. We can find the β (Table 2) within the range of 0.54×10^{-10} mW^{-1} to 2.12×10^{-10} mW^{-1} for the pure and doped samples. Similar to the photoluminescence spectra, we observe quenching occurring in the

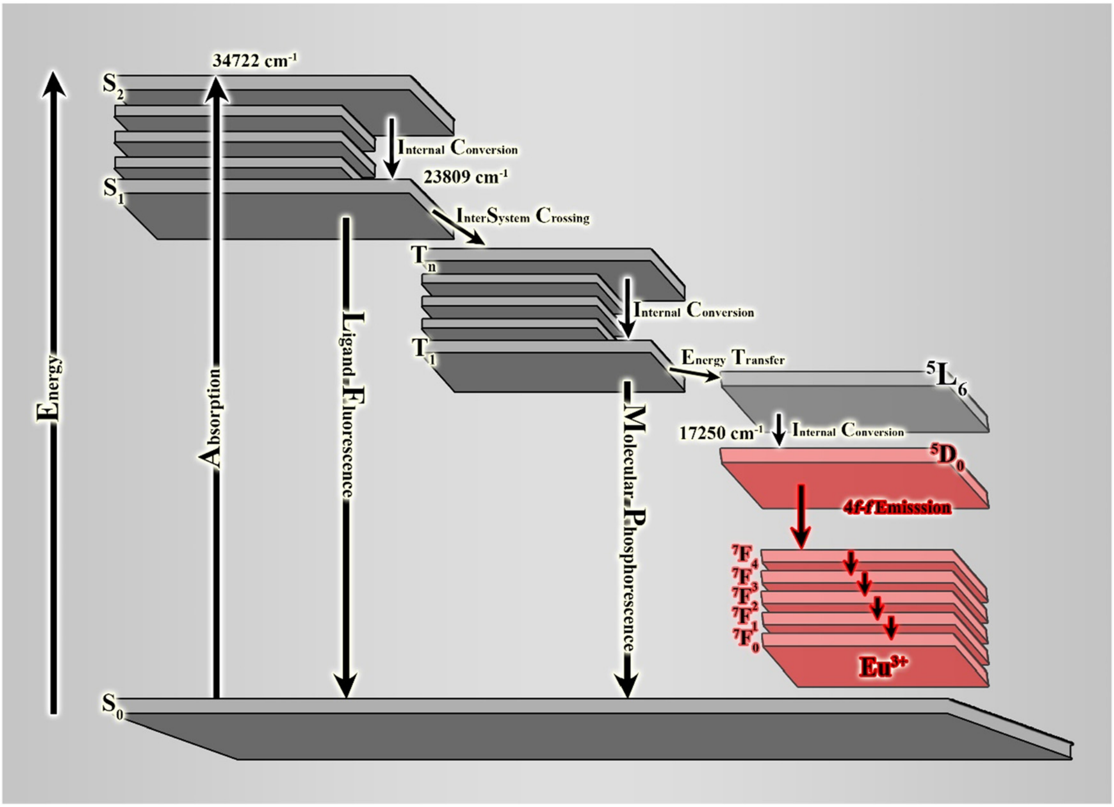

Fig. 9 Graphical representation of Jablonski's diagram.

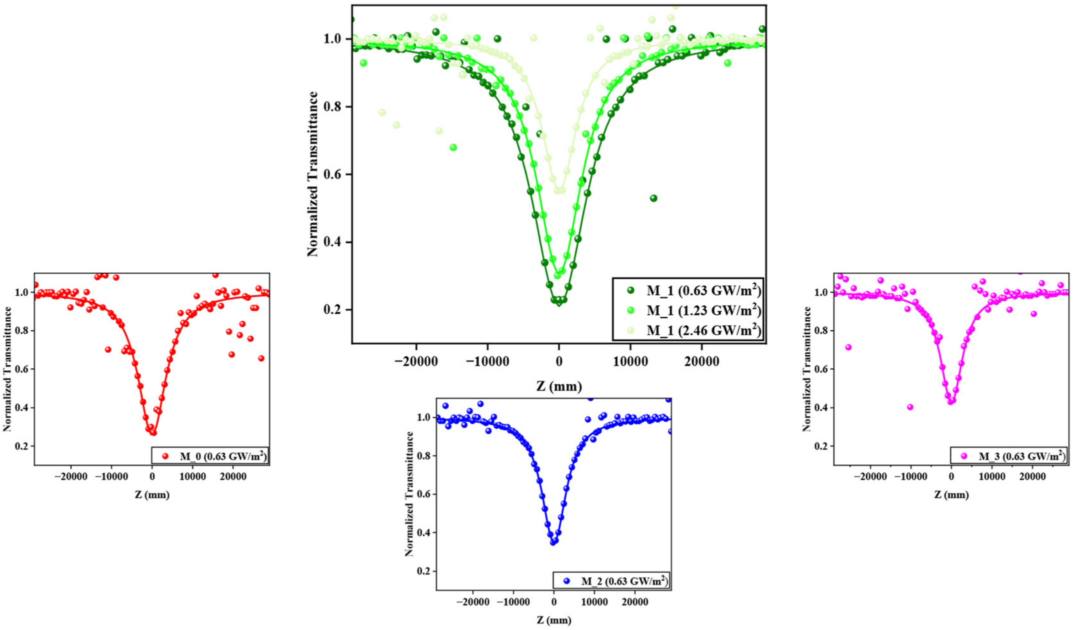

Fig. 10 Non-linear absorption of pure and doped MOF-5.

M_2 and M_3 samples, which confirms the quenching of light in the samples. Two-photon absorption can occur either through genuine 2PA (simultaneously absorbing two photons) or sequential 2PA (absorption of 1PA followed by ESA). In this work, the valley of the open aperture data is deeper and the value of β increases with the input intensity, which signatures

Table 2 NLO parameters of the pure and doped MOF-5

Samples and their intensity	Saturation intensity (10^{11} W m^{-2})	Nonlinear absorption co-efficient (10^{-10} mW^{-1})	Optical limiting threshold (10^{12} W m^{-2})
M_0 (0.63 GW m^{-2})	61	1.83	2.35
M_1 (0.63 GW m^{-2})	**74**	**2.12**	**1.53**
M_1 (1.23 GW m^{-2})	60	1.35	2.23
M_1 (2.46 GW m^{-2})	45	0.52	3.47
M_2 (0.63 GW m^{-2})	82	1.64	2.87
M_3 (0.63 GW m^{-2})	95	0.54	4.31

Table 3 Comparison of non-linear absorption co-efficient of various materials

S. no.	Material	Non-linear absorption co-efficient (β) (10^{-10} m W^{-1})	Ref.
1	2D-MoS$_2$	0.90	6
2	ZnO-TCO	1.10	8
3	LaPO$_4$	1.09	9
4	CePO$_4$	0.35	60
5	ZnMoO$_4$	0.50	67
6	MINB	0.70	68
7	2MIAB	0.58	69
8	rGO-ZnO	0.57	70
9	GO-PcZn	0.51	71
10	MOF-5	1.83	*present work
11	1% doped Eu-MOF-5	2.12	*present work
12	2% doped Eu-MOF-5	1.64	*present work
13.	3% doped Eu-MOF-5	0.54	*present work

the occurrence of a sequential 2PA process (Fig. 12). The obtained nonlinear absorption co-efficient for the sample M_1 shows superior reverse saturable absorption than M_0, M_2 and M_3. The included Eu^{3+} ions in the MOF act as trapped states and non-radiative centers in the host matrix, which increases the near-resonant state absorption. When increasing the Eu^{3+} ion concentration in the MOF, the lattice distortion occurring owing to dopant stress in the matrix suppresses the interband and intraband transitions, thereby decreasing the nonlinear absorption of M_2 and M_3. Hence, variation in the content of Eu^{3+} in the MOF can substantially influence the reverse saturable absorption and limiting behaviour of the material. The M_1 sample exhibited a β value of 2.12 × 10^{-10} mW^{-1}, and the doping of Eu^{3+} shows a 0.31 × 10^{-10} mW^{-1} increase in β value compared to that of pure MOF-5 (M_0). In comparison to the β values of various materials (Table 3), MOF-5 shows a better β value.

The electron in the M_1 sample, which is in the ground state (S$_0$), is excited by a photon with 2.33 eV and reaches the excited state (S$_1$), and as its bandgap is 3.78 eV, an additional photon is absorbed in the S$_1$ state to reach a virtual state. As a virtual state, the excited electron drops to the excitonic trapped state (S$_2$), followed by a non-radiative emission.[60] The M_1 sample (Fig. 10) showed an increase in transmittance value from 2.12 × 10^{-10} mW^{-1} to 1.35 × 10^{-10} mW^{-1} and 0.52 × 10^{-10} mW^{-1} when the intensity decreased from 0.63 GW m^{-2} to 1.23 GW m^{-2} and 2.46 GW m^{-2}, respectively.

As observed in absorption and emission analysis, the sample exhibits a visible emission state close to excitation (near-resonant state, 592 nm) and a strong UV absorption state (TPA state, 288 nm). These states involve themselves in non-linear absorption, resulting in a sequential TPA process. Further, the strong near-resonant state of the M_1 sample results in a stronger sequential two-photon absorption state with maximum β.

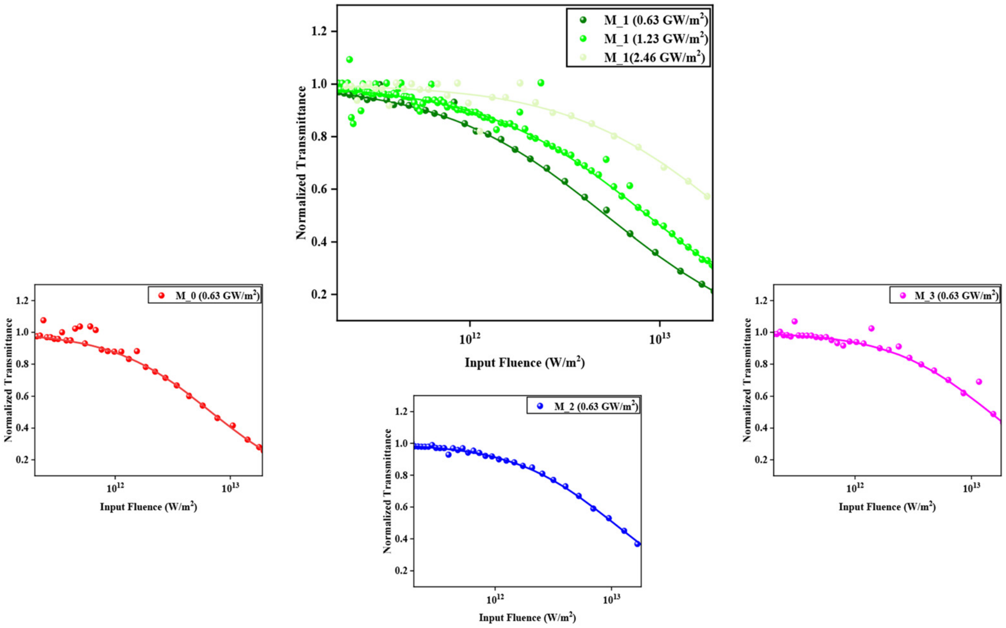

Fig. 11 Optical limiting studies of pure and doped MOF-5.

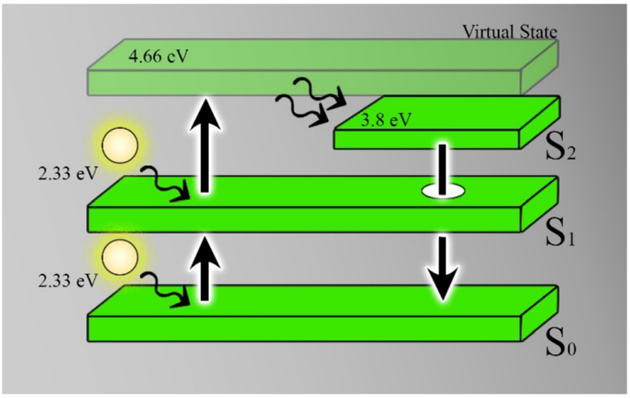

Fig. 12 Graphical representation of sequential two-photon absorption occurring in M_1 sample.

Optical limiting. The RSA nature of the samples led us to study the Optical Limiting (OL) properties. Upon interaction with the incident intense light (LASER), the NLO material (Optical Limiter) exhibits high transmittance at low power, whereas it does not transmit (attenuate) the higher power. The optical limiting response occurring owing to the non-linear absorbance of the high intensity light in the pure and doped MOF-5 samples can be attributed to the extended π-conjugated systems, which can facilitate energy transfer inside a molecule[72] and the NLO behaviour. The OL curve (Fig. 11) for pure and doped MOF-5 samples showing the incident energy flow at which the material's non-linear transmittance drops to half of the initial transmittance is known as the optical limiting threshold (OLT). The one that has a lower OLT is the effective optical limiter. The OLT of the pure MOF-5 (Table 2) is 2.35×10^{12} W m^{-2}, and on doping, the M_1 sample showed a decrease in OLT to 1.53×10^{12} W m^{-2}. However, the M_2 and M_3 samples show a huge increase in the OLT. Among the pure and doped MOF-5 samples, the M_1 sample shows the lowest optical limiting threshold, which means it has the highest optical limiting efficiency. When studying the intensity-dependent optical limiting threshold, we can observe that the optical limiting threshold increases depending on the intensity. Hence, the M_1 sample is suitable for laser safety devices that use 532 nm green lasers.

4. Conclusion

An effective method for synthesizing MOF-5 and introducing Eu^{3+} into MOF-5 is achieved using the solvothermal method, and its non-linear and photoluminescence studies reveal the quenching of optical properties when the doping concentration is increased. The XRD peaks, SEM images, and FTIR spectra reveal the structure, morphology and vibrational modes of the MOF-5. Non-linearity is found in the XRD parameters (M_2 and M_3 samples) caused by the larger ionic size of the Eu^{3+}. Raman studies using the 532 nm and 633 nm lasers confirm the presence of MOF-5. We also observe an overpowering of the PL background in the M_2 and M_3 samples. The presence of a second peak near 365 nm in the UV spectra explains the partial deterioration of MOF-5 to ZnO in M_2 and M_3. To unravel the decrease in crystallite size of the samples, we use photoluminescence studies, which explain red emission and confirm the presence of Eu^{3+}. Additionally, time-resolved photoluminescence studies were conducted to confirm the inability to undergo phosphorescence and remain in the fluorescence region owing to the inability of the linker to bond properly with the Eu^{3+} ions. The M_1 sample shows the saturation of the doping percentage, beyond which the doping causes the material to trap the light, not allowing the organic linker to excite Eu^{3+} ions through the antenna effect. The same behaviour of Eu^{3+}-doped MOF-5 in the non-linear range was observed while studying the non-linear absorption co-efficient. The linear absorption studies on the M_2 and M_3 samples show an extra bump near 365 nm, attributing to the partial deterioration in the structure, which clearly depends on the decreasing crystallite and grain size. The crystallite size and the grain size are directly dependent on the increase (M_1 sample) and quenching of light (M_2 and M_3 sample) in both the photoluminescence and non-linear absorption studies. The samples revealed reverse saturable absorption behaviour upon excitation, which can be attributed to the two-photon excitation occurring inside the material. The intensity-dependent study on sample M_1 verifies the presence of sequential two-photon absorption due to the change in the transmittance. The M_1 sample shows a maximum β value and low OLT, which is demonstrated as an optical limiter in safety goggles for various applications, including laser treatments in the medical field and targeting systems in the military. Hence, introducing Eu^{3+} to MOF-5 significantly improves the material properties.

Author contributions

Selva Boopalan A: conceptualization, data curation, methodology, and writing – original draft. Mani Rahulan K: formal analysis. Angeline Little Flower N: formal analysis. A. Dhanusha: data curation. Sabari Girisun T C: data curation and writing – review and editing. Annie Sujatha R: supervision, validation, visualization, and writing – review and editing.

Data availability

The data supporting this article have been included as part of the ESI.†

Conflicts of interest

There are no conflicts to declare.

Acknowledgements

We would like to acknowledge SRM Central Institution Facility (SCIF) and SRM Nanotechnology Research Centre (NRC) for providing the characterisation facility. The first author is thankful to SRMIST for providing the institute's doctoral fellowship.

References

1 P. A. Franken, A. E. Hill, C. E. Peters and G. Weinreich, *Phys. Rev. Lett.*, 1961, **7**(4), 118.
2 S. Ahmed, P. K. Cheng, J. Qiao, W. Gao, A. M. Saleque, M. N. Al Subri Ivan, T. Wang, T. I. Alam, S. U. Hani, Z. L. Guo and S. F. Yu, *ACS Nano*, 2022, **16**(8), 12390–12402.
3 S. U. Hani, S. Ahmed, T. I. Alam, A. M. Saleque, S. Saha, L. Xu and Y. H. Tsang, *Appl. Mater. Today*, 2025, **42**, 102555.
4 P. K. Cheng, S. Ahmed, J. Qiao, L. W. Wong, C. F. Yuen, A. M. Saleque, M. N. A. S. Ivan, S. U. Hani, M. I. Hossain, J. Zhao and Q. Wen, *Appl. Mater. Today*, 2022, **26**, 101296.
5 M. An, Z. Pan, X. Li, W. Wang, C. Jiang, G. Li, P. Guo, H. Lu, Y. Han, X. Chen and Z. Zhang, *ACS Appl. Mater. Interfaces*, 2022, **14**(48), 53971–53980.
6 R. Rafi, M. R. K, N. A. Little Flower, A. M, S. G. T. Chidambaram and A. S. Rajendran, *ACS Appl. Nano Mater.*, 2024, **7**(10), 11097–11106.
7 C. Nagarajan, V. Madhubala, P. Karuppasamy, P. Ramasamy and R. A. Sujatha, *Opt. Laser Technol.*, 2023, **159**, 108984.
8 A. Sahni, K. M. Rahulan, N. A. L. Flower, T. S. Girisun, M. Abith and R. A. Sujatha, *Surf. Interfaces*, 2024, **45**, 103800.
9 B. Vijayakumar, K. M. Rahulan, R. A. Sujatha, M. Durairaj, T. S. Girisun and N. A. L. Flower, *J. Photochem. Photobiol., A*, 2023, **439**, 114615.
10 L. Gao, B. Li, H. Yi, J. Cui, L. Yang, Y. Song, H. R. Yang, L. Zhou and S. Fang, *ACS Omega*, 2022, **7**(32), 27959–27968.
11 O. M. Yaghi and H. Li, *J. Am. Chem. Soc.*, 1995, **117**(41), 10401–10402.
12 H. Li, M. Eddaoudi, M. O'Keeffe and O. M. Yaghi, *Nature*, 1999, **402**(6759), 276–279.
13 J. Li, S. Cheng, Q. Zhao, P. Long and J. Dong, *Int. J. Hydrogen Energy*, 2009, **34**(3), 1377–1382.
14 L. C. Lin, D. Paik and J. Kim, *Phys. Chem. Chem. Phys.*, 2017, **19**(18), 11639–11644.
15 R. Xavier and K. Sivaperuman, *Mater. Today Commun.*, 2023, 107831.
16 N. T. Phan, K. K. Le and T. D. Phan, *Appl. Catal., A*, 2010, **382**(2), 246–253.
17 L. Zhang, Y. Chen, R. Shi, T. Kang, G. Pang, B. Wang, Y. Zhao, X. Zeng, C. Zou, P. Wu and J. Li, *Inorg. Chem. Commun.*, 2018, **96**, 20–23.
18 A. J. Graham, D. R. Allan, A. Muszkiewicz, C. A. Morrison and S. A. Moggach, *Angew. Chem., Int. Ed.*, 2011, **50**(47), 11138–11141.
19 C. R. Marshall, S. A. Staudhammer and C. K. Brozek, *Chem. Sci.*, 2019, **10**(41), 9396–9408.
20 S. Ehrling, H. Miura, I. Senkovska and S. Kaskel, *Trends Chem.*, 2021, **3**(4), 291–304.
21 N. D. H. Gamage, K. A. McDonald and A. J. Matzger, *Angew. Chem., Int. Ed.*, 2016, **55**(39), 12099–12103.
22 S. Goktas, A. Tumbul and A. Goktas, *J. Supercond. Novel Magn.*, 2023, **36**(10), 1875–1892.
23 Z. Aba, A. Goktas and A. Kilic, *J. Sol-Gel Sci. Technol.*, 2024, **109**(1), 260–271.
24 N. A. Rodríguez, R. Parra and M. A. Grela, *RSC Adv.*, 2015, **5**(89), 73112–73118.
25 G. Sahin, A. Goktas and E. Aslan, *J. Sol-Gel Sci. Technol.*, 2024, **112**(2), 425–443.
26 A. Tumbul, E. Aslan, A. Göktaş, I. H. Mutlu, F. Arslan and F. Aslan, *Appl. Phys. A*, 2024, **130**(4), 225.
27 A. Goktas, S. Modanlı, A. Tumbul and A. Kilic, *J. Alloys Compd.*, 2022, **893**, 162334.
28 H. A. Ozen, B. Ozturk and H. Obekcan, *Nevsehir Bilim ve Teknoloji Dergisi*, 2017, **6**, 415–423.
29 Z. Zhao, X. Ma, Z. Li and Y. S. Lin, *J. Membr. Sci.*, 2011, **382**(1–2), 82–90.
30 C. Xia, C. Yu, M. Cao, J. Xia, D. Jiang, G. Zhou, D. Zhang and H. Li, *Ceram. Int.*, 2018, **44**(17), 21040–21046.
31 K. Binnemans, *Chem. Rev.*, 2009, **109**(9), 4283–4374.
32 M. Ahmadi, S. M. Ayyoubzadeh, F. Ghorbani-Bidkorbeh, S. Shahhosseini, S. Dadashzadeh, E. Asadian, M. Mosayebnia and S. Siavashy, *Heliyon*, 2021, **7**(4), e06914.
33 N. T. Binh, D. M. Tien, L. T. K. Giang, H. T. Khuyen, N. T. Huong, T. T. Huong and T. Dai Lam, *Mater. Chem. Phys.*, 2014, **143**(3), 946–951.
34 S. Mishra, S. Rakshit and N. Goel, *Talanta Open*, 2024, 100329.
35 S. Goktas and A. Goktas, *J. Alloys Compd.*, 2021, **863**, 158734.
36 J. S. Choi, W. J. Son, J. Kim and W. S. Ahn, *Microporous Mesoporous Mater.*, 2008, **116**(1–3), 727–731.
37 K. K. Gangu, S. Maddila and S. B. Jonnalagadda, *RSC Adv.*, 2022, **12**(22), 14282–14298.
38 T. M. Reineke, M. Eddaoudi, M. O'keeffe and O. M. Yaghi, *Angew. Chem., Int. Ed.*, 1999, **38**(17), 2590–2594.
39 M. Alvaro, E. Carbonell, B. Ferrer, F. X. Llabrés i Xamena and H. Garcia, *Chem. – Eur. J.*, 2007, **13**(18), 5106–5112.
40 J. A. Botas, G. Calleja, M. Sánchez-Sánchez and M. G. Orcajo, *Langmuir*, 2010, **26**(8), 5300–5303.
41 C. S. Patil, Q. M. Saqib, J. Kim, M. Noman, S. R. Patil, Y. Ko, M. D. Kurkuri and J. Bae, *Adv. Comp., Hybrid Mater.*, 2024, **7**(5), 1–22.
42 Y. Tang, H. Wu, W. Cao, Y. Cui and G. Qian, *Adv. Opt. Mater.*, 2021, **9**(23), 2001817.
43 J. Ren, T. Li, X. Zhou, X. Dong, A. V. Shorokhov, M. B. Semenov, V. D. Krevchik and Y. Wang, *Chem. Eng. J.*, 2019, **358**, 30–39.
44 M. Fiaz, M. Kashif, M. Fatima, S. R. Batool, M. A. Asghar, M. Shakeel and M. Athar, *Catal. Lett.*, 2020, **150**, 2648–2659.

45 S. Hausdorf, J. Wagler, R. Moβig and F. O. Mertens, *J. Phys. Chem. A*, 2008, **112**(33), 7567–7576.

46 J. Hafizovic, M. Bjørgen, U. Olsbye, P. D. Dietzel, S. Bordiga, C. Prestipino, C. Lamberti and K. P. Lillerud, *J. Am. Chem. Soc.*, 2007, **129**(12), 3612–3620.

47 S. Dhara, K. Imakita, M. Mizuhata and M. Fujii, *Nanotechnology*, 2014, **25**(22), 225202.

48 S. Göktaş, *Chem. Afr.*, 2024, **7**, 4425–4437.

49 H. F. Greer, Y. Liu, A. Greenaway, P. A. Wright and W. Zhou, *Cryst. Growth Des.*, 2016, **16**(4), 2104–2111.

50 G. Şahin and S. Göktaş, *Gazi J. Eng. Sci.*, 2024, **10**(1).

51 G. Kumar and D. T. Masram, *ACS Omega*, 2021, **6**(14), 9587–9599.

52 M. Müller, S. Turner, O. I. Lebedev, Y. Wang, G. Van Tendeloo and R. A. Fischer, *Eur. J. Inorg.*, 2011, 1876–1887.

53 A. Mariscal, A. Quesada, A. T. Martín-Luengo, M. A. García, A. Bonanni, J. F. Fernández and R. Serna, *Appl. Surf. Sci.*, 2018, **456**, 980–984.

54 H. Asadevi, P. Prasannakumaran Nair Chandrika Kumari, R. Padmavati Amma, S. A. Khadar, S. Charivumvasathu Sasi and R. Raghunandan, *ACS Omega*, 2022, **7**(15), 13031–13041.

55 B. X. Vuong, *J. Sci. Technol.*, 2016, 46–49.

56 R. Sabouni, H. Kazemian and S. Rohani, *Chem. Eng. J.*, 2010, **165**(3), 966–973.

57 L. Huang, H. Wang, J. Chen, Z. Wang, J. Sun, D. Zhao and Y. Yan, *Microporous Mesoporous Mater.*, 2003, **58**(2), 105–114.

58 S. Bordiga, C. Lamberti, G. Ricchiardi, L. Regli, F. Bonino, A. Damin, K. P. Lillerud, M. Bjorgen and A. Zecchina, *Chem. Commun.*, 2004, **1**(20), 2300–2301.

59 Y. Zhou and C. J. Liu, *Plasma Chem. Plasma Process.*, 2011, **31**, 499–506.

60 B. Vijayakumar, K. M. Rahulan, R. A. Sujatha, M. Durairaj, T. C. Girisun, N. Flower and A. Little, *ACS Appl. Nano Mater.*, 2023, **6**(9), 7499–7509.

61 M. D. Allendorf, C. A. Bauer, R. K. Bhakta and R. J. T. Houk, *Chem. Soc. Rev.*, 2009, **38**(5), 1330–1352.

62 B. M. Sánchez-fabila, S. Loera-Serna and I. A. Garduño-Wilches, *J. Innovative Eng.*, 2023, **7**(20), 7–15.

63 N. T. Binh, D. M. Tien, L. T. K. Giang, H. T. Khuyen, N. T. Huong, T. T. Huong and T. Dai Lam, *Mater. Chem. Phys.*, 2014, **143**(3), 946–951.

64 V. Villemot, M. Hamel, R. B. Pansu, I. Leray and G. H. Bertrand, *RSC Adv.*, 2020, **10**(31), 18418–18422.

65 A. S. Jayasree, N. A. L. Flower, R. A. Sujatha, M. Durairaj, T. S. Girisun and K. M. Rahulan, *Appl. Phys. A*, 2024, **130**(3), 181.

66 K. Sowmiya, S. Buvaneswaran, T. S. Girisun and B. Gunasekaran, *Opt., Quantum Electron.*, 2024, **56**(9), 1412.

67 K. Sowmiya, S. Buvaneswaran, T. Sahoo, S. G. Tc and B. Gunasekaran, *Opt. Mater.*, 2024, **147**, 114769.

68 M. K. Kavitha, H. John, P. Gopinath and R. Philip, *J. Mater. Chem. C*, 2013, **1**(23), 3669–3676.

69 J. Zhu, Y. Li, Y. Chen, J. Wang, B. Zhang, J. Zhang and W. J. Blau, *Carbon*, 2011, **49**(6), 1900–1905.

70 Y. Liang, W. Hu, X. Yuan, Z. Zeng, B. Zhu and Y. Gu, *Adv. Opt. Mater.*, 2022, **10**(18), 2200779.

71 M. Sheik-Bahae, A. A. Said, T. H. Wei, D. J. Hagan and E. W. Van Stryland, *SPIE Milestone Ser.*, 2003, **174**, 292–301.

72 L. Gao, B. Li, H. Yi, J. Cui, L. Yang, Y. Song, H. R. Yang, L. Zhou and S. Fang, *ACS Omega*, 2022, **7**(32), 27959–27968.